Neurofibrillary tangle-bearing neurons are functionally integrated in cortical circuits in vivo

Neurofibrillary tangle-bearing neurons are functionally integrated in cortical circuits in vivo

Kishore V. Kuchibhotla[a,b,1], Susanne Wegmann[a,1], Katherine J. Kopeikina[a,c], Jonathan Hawkes[a], Nikita Rudinskiy[a], Mark L. Andermann[d], Tara L. Spires-Jones[a,e], Brian J. Bacskai[a], and Bradley T. Hyman[a,2]

[a]Alzheimer's Disease Research Laboratory, Department of Neurology, MassGeneral Institute for Neurodegenerative Disease, Massachusetts General Hospital, Harvard Medical School, Charlestown, MA 02129; [b]Skirball Institute, NYU School of Medicine, New York, NY 10016; [c]Department of Anatomy and Neurobiology, Boston University School of Medicine, Boston, MA 02118; [d]Division of Endocrinology, Department of Medicine, Beth Israel Deaconess Medical Center, Harvard Medical School, Boston, MA 02215; and [e]Centre for Cognitive and Neural Systems, University of Edinburgh Neuroscience, Edinburgh EH8 9JZ, United Kingdom

Edited by Paul Greengard, The Rockefeller University, New York, NY, and approved November 22, 2013 (received for review October 7, 2013)

Alzheimer's disease (AD) is pathologically characterized by the deposition of extracellular amyloid-β plaques and intracellular aggregation of tau protein in neurofibrillary tangles (NFTs) (1, 2). Progression of NFT pathology is closely correlated with both increased neurodegeneration and cognitive decline in AD (3) and other tauopathies, such as frontotemporal dementia (4, 5). The assumption that mislocalization of tau into the somatodendritic compartment (6) and accumulation of fibrillar aggregates in NFTs mediates neurodegeneration underlies most current therapeutic strategies aimed at preventing NFT formation or disrupting existing NFTs (7, 8). Although several disease-associated mutations cause both aggregation of tau and neurodegeneration, whether NFTs per se contribute to neuronal and network dysfunction in vivo is unknown (9). Here we used awake in vivo two-photon calcium imaging to monitor neuronal function in adult rTg4510 mice that overexpress a human mutant form of tau (P301L) and develop cortical NFTs by the age of 7–8 mo (10). Unexpectedly, NFT-bearing neurons in the visual cortex appeared to be completely functionally intact, to be capable of integrating dendritic inputs and effectively encoding orientation and direction selectivity, and to have a stable baseline resting calcium level. These results suggest a reevaluation of the common assumption that insoluble tau aggregates are sufficient to disrupt neuronal function.

paired helical filaments | tau pathology | neuronal networks

Neurofibrillary tangles (NFTs) containing aggregated tau protein (1) have long been considered key players in the progressive neural dysfunction and neurodegeneration observed in Alzheimer's disease (AD) (2, 3) and other tauopathies (4, 5). It is commonly assumed that NFT-bearing neurons exhibit deficits in synaptic integration and eventually lead to neurodegeneration (11, 12). However, the actual functional properties of NFT-bearing neurons in intact neural circuits have not been explored previously (13). We addressed this question directly using awake in vivo two-photon calcium imaging in a mouse model of NFT formation (rTg4510) by applying recently developed imaging approaches allowing for single-neuron–level and population-level assessment of neural activity in awake mice (14). Because two-photon calcium imaging allows for measurement of response properties in many neurons simultaneously, we were able to directly isolate the impact of NFT deposition in a neuronal microcircuit by evaluating population-level network dynamics and, more specifically, by differentiating the function of individual NFT-bearing and neighboring non–NFT-bearing neurons.

To assess the functional properties of neurons in the visual cortex, we used a genetically encoded ratiometric calcium indicator, yellow cameleon 3.6 (YC3.6), packaged in an adeno-associated viral vector (15, 16). To assess functional responses, we exploited the well-characterized functional architecture of visual cortex whereby neurons in mouse visual cortex modulate their activity during presentation of drifting gratings moving at specific orientations and directions (orientation and direction selectivity) (17, 18). We further used YC3.6 as a FRET-based ratiometric indicator to make quantitative measurements of resting calcium (15). Resting calcium is tightly regulated in the brain, and slight deviations can trigger chronic and severe degenerative pathways (15). Thus, measurement of resting calcium is an important and complementary functional assay for evaluating neuronal health. Importantly, performing experiments in awake, head-fixed animals eliminates the impact of anesthesia on response properties, resting calcium, and tau aggregation (Fig. 1 *A* and *B* and Movie S1) (19).

Results

We first confirmed that 8- to 10-mo-old control animals exhibited robust orientation and direction selectivity, similar to previous reports in young and aged mice (20) (Fig. 1 and Fig. 2 *B–E*, control traces). Average and single trial traces of responses to visual stimuli measured in a single neuron from a control animal are shown in Fig. 1*C*. In this example, the neuron (cell 1) preferentially responds to a visual stimulus orientation of 225° and has an orientation selectivity index (OSI) of 0.95 and a direction selectivity index (DSI) of 0.95 (Fig. 1 *C*, *D*, and *F*; 0 indicates no selectivity, and 1 indicates perfect selectivity).

Significance

Alzheimer's disease is pathologically characterized by extracellular amyloid-β plaques and intracellular neurofibrillary tangles (NFTs). It has long been assumed that the accumulation of tau into NFTs causes neuronal dysfunction and death, and is a proximate cause of dementia in patients with Alzheimer's disease. This assumption underlies the NFT-busting drugs currently in clinical trials and research efforts aimed at understanding tau aggregation. Our study tested the dogma that NFT-bearing neurons are indeed impaired in their ability to respond to complex sensory stimuli. Using two-photon imaging in awake mice with NFT pathology, we found that individual neurons with NFTs respond to visual stimuli and do not impair local circuits. These unexpected results suggest that the presence of an NFT does not inevitably lead to gross physiological alterations.

Author contributions: K.V.K., S.W., T.L.S.-J., B.J.B., and B.T.H. designed research; K.V.K., S.W., K.J.K., J.H., and N.R. performed research; K.V.K., S.W., M.L.A., and T.L.S.-J. contributed new reagents/analytic tools; K.V.K. and S.W. analyzed data; and K.V.K., S.W., B.J.B., and B.T.H. wrote the paper.

The authors declare no conflict of interest.

This article is a PNAS Direct Submission.

Freely available online through the PNAS open access option.

[1]K.V.K. and S.W. contributed equally to this work.

[2]To whom correspondence should be addressed. E-mail: bhyman@partners.org.

This article contains supporting information online at www.pnas.org/lookup/suppl/doi:10.1073/pnas.1318807111/-/DCSupplemental.

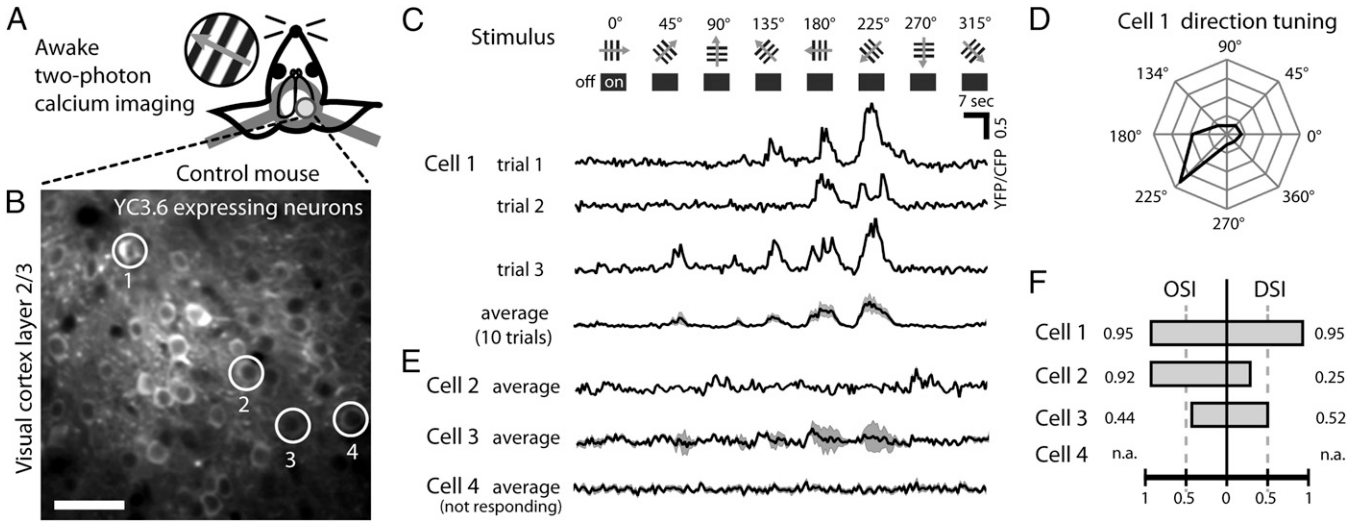

Fig. 1. YC3.6 calcium imaging in awake cortex of control mice reveals robust visual response tuning. (*A*) Awake and head-fixed mice expressing AAV-YC3.6 in visual cortex were presented with drifting gratings to record visually evoked calcium responses through a chronic cranial window (Movie S1). (*B*) In vivo two-photon image of YC3.6-expressing neurons in layer 2/3 (~180 μm below the brain surface) with four example neurons (white circles). (Scale bar: 50 μm.) (*C*) Drifting gratings (eight stimulus types, 45° apart) were presented for 7–10 s, followed by 7–10 s without stimulation (gray screen). This sequence was repeated 10 times. For cell 1 (orientation- and direction-selective), three representative single-trial time courses (YFP:CFP ratio) and the average trace across 10 trials reveal its predominant response to a grating direction of 225°. SEM is shown in gray; arrowhead indicates preferred direction. (*D*) Polar plot of cell 1 demonstrating selectivity of this neuron for the 225° stimuli. (*E*) Average traces of three other neurons (white circles in *A*) illustrate the diversity in orientation and direction tuning. Cell 2 is orientation-selective but not direction-selective, cell 3 responds to all directions (broadly tuned), and cell 4 does not respond to any direction (not responding). (*F*) OSI and DSI for cells 1–4.

We next explored the functional response profiles of neurons in the visual cortex of transgenic mice with a significant NFT load in the visual cortex at similar ages to control animals (Fig. 2*A* and Fig. S1) and compared these profiles with those of neurons from control brains (Fig. 2 *B*–*E*). The rTg4510 mice exhibited numerous NFTs throughout the cortex, including the visual cortex (Fig. 2*A*), along with behavioral deficits typically seen at this age (10). We observed a marked uniformity in resting calcium levels across the population of neurons measured in control mice (Fig. 2*B*), consistent with previous reports of tightly regulated resting calcium concentration in the healthy cortex (15). Neurons in the rTg4510 mice and control mice exhibited nearly identical resting calcium profiles (control, 1.32; rTg4510, 1.31; cohort-level: $P = 0.84$, t test, $n = 3$ rTg4510 mice, $n = 3$ control mice; cell-specific: $P = 0.22$, Mann–Whitney U test, $n = 898$ rTg4510 neurons, $n = 329$ control neurons) (Fig. 2*B*).

We further explored whether other cortical brain regions exhibited disrupted calcium homeostasis by measuring resting calcium outside of the visual cortex (somatosensory areas), and found no significant difference (Fig. S2). Moreover, neurons in mice with a high NFT load exhibited the same robust visual responses (Fig. 2 *C*–*E*) as were observed in controls including many neurons with sharp orientation and direction selectivity (OSI: $P = 0.47$, DSI: $P = 0.82$, Student t test; $n = 6$ Tg4510 mice, $n = 6$ control mice) (Fig. 2 *D* and *E* and Fig. S3). Based on these data, we conclude that the neuronal network in the visual cortex of mice with a high NFT load appears to be functionally intact and comparable to that of control animals.

To examine whether disrupted calcium homeostasis or altered neuronal tuning in NFT-bearing neurons was masked by averaging the functional properties across all neurons and mice, we next compared resting calcium regulation and neuronal tuning in individual neurons with or without NFTs (Fig. 3). To identify NFT-bearing neurons in the visual cortex of rTg4510 mice, we aligned images obtained in vivo with images of the same neurons obtained by postmortem labeling for markers of NFTs (Fig. 3 *A*–*C*) (21). The mice were perfused with paraformaldehyde (PFA) immediately after completion of in vivo imaging, followed by postmortem immunolabeling of YC3.6 (with anti-GFP antibody), hyperphosphoryated tau (with PHF1 antibody), and staining of mature NFTs using thioflavin-S (ThioS) in whole brains of rTg4510 mice (Fig. S4). All ThioS-positive NFT-bearing neurons ($n = 32$) showed PHF1 labeling of hyperphosphorylated tau, and very few neurons ($n = 6$) had hyperphosphorylated tau but no mature NFTs. For statistical analyses of NFT neuron responsiveness, ThioS stained cells were defined as NFT-bearing neurons. In a subset of animals, we also labeled NFTs in vivo using i.v. injections of the Congo red derivate methoxy-X04 in anesthetized animals (22, 23) (Fig. S5).

Remarkably, resting calcium (Fig. 3*D*) and neuronal tuning (Fig. 3 *G* and *H*) were very similar in nearby (and often neighboring) NFT-bearing and non–NFT-bearing neurons from the same animal and at the same imaging volume. Average resting calcium levels were nearly identical, and resting calcium distributions of neighboring NFT-bearing neurons did not exhibit elevated calcium levels compared with nearby non–NFT-bearing neurons [n = 13-110 NFT-bearing neurons (per mouse), n = 22-1006 non-NFT bearing neurons (per mouse), $n = 3$ mice; $P = 0.99$ for NFT vs. non-NFT within each animal, Mann-Whitney U test; $P = 0.24$ across cohort, paired t test]. In addition, we found no difference between resting calcium levels in NFT-bearing and non–NFT-bearing neurons in other areas of the somatosensory cortex (Fig. S6). For neuronal responsiveness to visual stimuli, we detected no difference in the probability of response ($n = 142$ NFT-bearing neurons, $n = 1{,}602$ non-NFT-bearing neurons, $n = 3$ mice; $P = 0.39$, Student t test), orientation selectivity, or direction selectivity ($n = 24$ NFT-bearing neurons, $n = 122$ non–NFT-bearing neurons, $n = 3$ mice; OSI, $P = 0.38$, DSI, $P = 0.36$, two-way ANOVA) (Fig. 3 *F*–*H*). For OSI and DSI, we performed statistic analyses across the cohort of three animals (Avg) and for each individual animal (Ms1–Ms3), to reduce any cohort-level averaging that might have obscured potential differences (*Materials and Methods*).

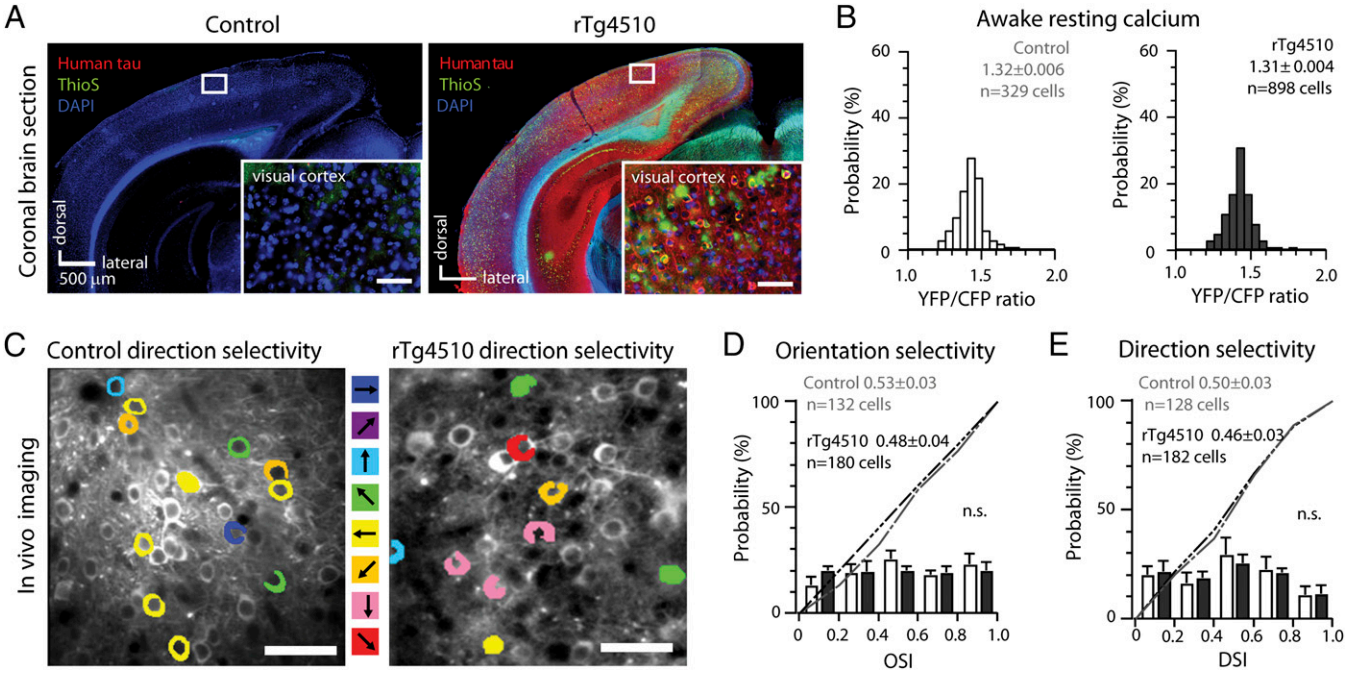

Fig. 2. The visual cortex of mice with a severe NFT load appears functionally intact. (*A*) Coronal brain sections demonstrate human tau protein expression (immunolabeled with Tau13) and severe NFT deposition (ThioS) in the visual cortex of rTg4510 mice (*Right*), but not of control mice (*Left*), at age 9 mo. (*B*) Distributions of average resting calcium levels (YFP:CFP ratios) determined from the time intervals between stimuli reveal no significant difference ($P = 0.84$, *t* test) between control mice ($n = 3$) and rTg4510 mice ($n = 3$). Moreover, there is no significant difference when comparing at a cell-specific level ($P = 0.22$, Mann–Whitney *U* test; $n = 898$ rTg4510 cells, n = 329 control cells). (*C*) Neurons in visual cortex layer 2/3 of both control and NFT-loaded rTg4510 mice show robust direction preferences (DSI >0.5). Pseudocolors denote the preferred stimulus direction of tuned cells; noncolored cells were not responsive or broadly tuned. (Scale bar: 50 μm.) (*D* and *E*) Distributions of OSI (*D*) and DSI (*E*) show no significant difference between orientation selectivity (OSI: $P = 0.47$, *t* test) and direction selectivity (DSI: $P = 0.82$, *t* test) of responding neurons from rTg4510 mice ($n = 6$) with a high NFT load and control mice ($n = 6$). Dashed lines indicate cumulative probabilities.

Discussion

NFT-bearing neurons are characterized by abnormal accumulation of fibrillar tau aggregates in the cell soma and proximal dendrites compared with the predominantly axonal localization of tau in healthy neurons (24). To isolate the consequences of tau aggregation and mislocalization to soma and dendrites (6), we focused on the primary visual cortex, a brain area in which the major driving input source, the lateral geniculate nucleus, is structurally intact (10, 25) (Fig. S7). We found that in the visual cortex, neurons containing conspicuous quantities of mislocalized and aggregated tau nonetheless appear to have a normal capacity to integrate dendritic inputs and respond robustly to visual stimuli and also maintain normal somatic baseline calcium levels. In particular, we show that individual NFT-bearing neurons can respond robustly after integrating sensory inputs and are functionally indistinguishable from neighboring non–NFT-bearing neurons. These results demonstrate that NFT-bearing neurons remain functionally integrated in cortical circuits.

The possibility remains that network elements downstream of NFT-bearing neurons may show deficits linked to axonal or presynaptic deficits arising from NFT-bearing neurons. This property may be particularly relevant in neurons with longer axonal projections. Moreover, although our findings suggest that NFT-bearing neurons are capable of integrating sensory inputs, the possibility exists that a more sensitive assay that challenges NFT-bearing neurons may reveal subtle alterations in neuronal function. It also is possible that NFT deposition exerts deleterious effects on neural system function at later stages in the disease; however, similar assays as those used in the present study have identified dysfunctional phenotypes in amyloid mouse models with clearly impaired neuronal tuning in animals with amyloid plaques (20) and profound alterations in baseline resting calcium levels (15).

In combination with a previous study showing that NFT-bearing neurons in the hippocampus of rTg4510 mice can induce expression of the immediate early gene *Arc* after behavioral stimulation (26) and another study showing relatively normal electrophysiological properties in an acute slice preparation (13), our results strengthen the hypothesis that NFT deposition resembles an "off-pathway" disease side effect that in itself does not cause significant disruption of network function (9, 10, 13, 27–29). Mouse models are inherently limited in their ability to capture all aspects of adult human AD because of differences in pathology structure, kinetics, and distribution. Future work will need to explore the longitudinal impact of tau deposition on single-neuron, local circuit, and neural system function: how neurons and networks change before, during, and after NFT deposition, and how prefibrillar and soluble oligomeric tau aggregates impact neuronal function. These types of studies will benefit greatly from new in vivo staining compounds that differentially bind soluble, prefibrillar, and aggregated tau. Even within these limitations, however, our present findings call into question therapeutic strategies aimed at preventing or disrupting fibrillar tau deposits (30), which may indeed sequester more toxic soluble tau species (31, 32).

Materials and Methods

Animals. All experiments were performed using 8- to 10-mo-old transgenic rTg4510 mice overexpressing full-length human four-repeat tau (0N4R) carrying the frontotemporal dementia-associated P301L mutation (10). By age 7–8 mo, rTg4510 mice had developed a large number of NFTs in the cortex. Control animals lacked the human tau transgene.

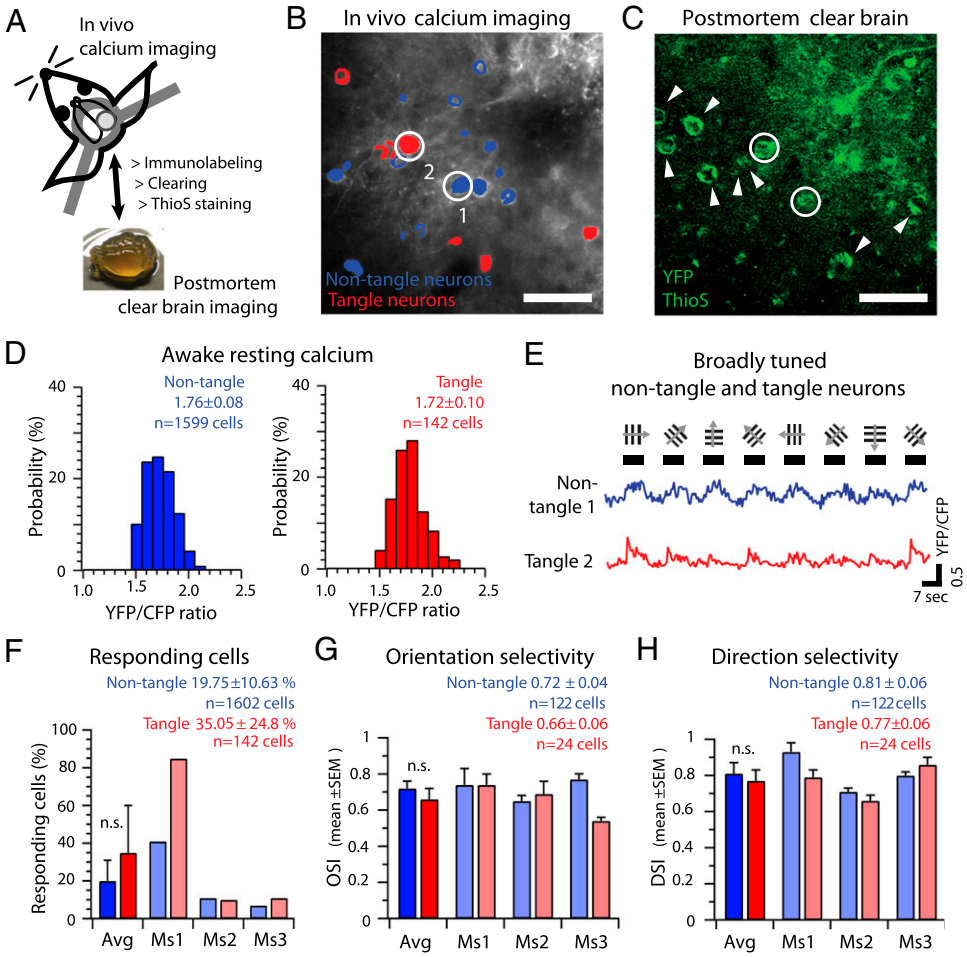

Fig. 3. NFT-bearing neurons exhibit normal visual response properties. (*A*) In vivo imaging sites were coregistered with postmortem images obtained from cleared brains in which neurons were labeled for YC3.6 (immunolabeled with anti-GFP) and NFTs (staining with ThioS; detailed workflow in Fig. S4). (*B*) In vivo image showing neighboring NFT-free (blue) and NFT-bearing (red) neurons, including two visually responsive neurons (white circles). (Scale bar: 50 μm.) (*C*) The presence of NFTs (white arrowheads) was identified based on postmortem NFT staining in clear brain. (Scale bar: 50 μm.) (*D*) Resting calcium distributions of non–NFT-bearing and NFT-bearing neurons in the visual cortex show no significant difference [cohort-level, paired *t* test, $n = 3$ mice; $P = 0.24$; intra-animal, Mann-Whitney U test right-sided, n = 13-110 NFT-bearing neurons (per mouse), n = 22-1006 non-NFT bearing neurons (per mouse), $P = 0.99$]. (*E*) Average response traces of a broadly tuned non–NFT-bearing neuron and an NFT-bearing neuron (white circles in *B* and *C* labeled 1 and 2, respectively). (*F*) The average percentage of responding neurons (mean ± SEM) was not significantly different between non–NFT-bearing (blue, 1602 cells) and NFT-bearing (red, 142 cells) neurons ($P = 0.4$, Student *t* test; $n = 3$ mice), but was highly variable among mice (Ms1–Ms3). (*G* and *H*) Average (mean ± SEM) OSI (*G*) and DSI (*H*) of non–NFT-bearing (blue) and NFT-bearing (red) neurons, analyzed across all mice (Avg) and for intramouse comparisons (Ms1–Ms3) (two-way ANOVA with Tukey–Cramer post hoc test; $n = 24$ NFT-bearing neurons, $n = 122$ non–NFT-bearing neurons; 3 mice; OSI: $P = 0.4$ for NFT, $P = 0.3$ for interaction; DSI: $P = 0.4$ for NFT, $P = 0.3$ for interaction).

Surgical Procedures. A small craniotomy was performed over the visual cortex (15, 33). An adeno-associated virus (AAV) vector encoding the ratiometric calcium indicator YC3.6 (AAV8-CBA-YC3.6; Penn Vector Core) was stereotactically injected for expression of YC3.6 in layer 2/3 neurons in the right primary visual cortex V1 (from lambda: +0.5 mm anteroposterior, 2.7 mm lateral, 0.6 mm dorsoventral). Above the injection coordinates, a cranial window was implanted replacing a circular piece (3 mm diameter) of skull by a glass coverslip that was secured in place using a mix of dental cement and Krazy Glue. A custom-made stainless-steel headpost (Ponoko) was affixed to the skull using C&B Metabond dental cement (Parkell), and each animal was allowed to recover for at least 2–3 wk. Before imaging, animals were habituated to the custom-made head-fixation device (Thorlabs posts and Altos head clamps), during which they were allowed to run freely on a circular treadmill (Ponoko).

In Vivo Calcium Imaging. Two-photon fluorescence of YC3.6 was excited at 860 nm using a mode-locked Ti:sapphire laser (MaiTai; Spectra Physics) and detected in the blue channel (CFP emission) and the yellow channel (YFP emission). Imaging was performed with a multiphoton imaging system (Fluoview1000; Olympus) equipped with a water immersion objective (25×, NA = 1.05; Olympus), with the emission path shielded from external light contamination. To record time courses of visually stimulated neuronal activity-dependent calcium levels, awake animals were head-fixed under the microscope, and an LCD monitor displaying the visual stimuli was placed in front of the left eye (screen–eye distance, ~20 cm; screen-midline angle, 60°). Visual stimuli were drifting (2 Hz) sine-wave gratings (80% or 100% contrast, black and white) presented for ~7 s. Stimuli were presented at 60 Hz using a calibrated 19-inch LCD monitor (Viewsonic VP930B). Eight stimuli (at 45° orientation increments) were presented sequentially in counterclockwise order with ~7 s between stimuli. During visual stimulation, several ~300 μm^2 areas in layer 2/3 of V1 containing multiple YC3.6-expressing neurons were selected and imaged (scan rate, ~2.5 Hz, 0.429 s/frame; laser power, ≤50 mW).

Image Processing and Data Analysis. Semiautomated data analysis was performed using custom-written software in ImageJ (National Institutes of Health) and MATLAB (MathWorks). Images were aligned for minor shifts in the *x-y* plane owing to movement, cellular regions of interest (ROI) were manually drawn, YFP:CFP ratios were created and spatially filtered, and raw time courses were extracted. Images were excluded if there was a significant

shift in the *z*-axis (rare; <5% of all time courses). For each cellular ROI, the change in directional response (ΔR; $R - R_{nonstimulated}$) was compared across directions and against background, and "responsive" cells were identified ($P < 0.05$, ANOVA with the Tukey–Cramer post hoc test and Bonferonni correction). Only responsive cells were used for further analysis of orientation and direction tuning.

The OSI and DSI were calculated as described previously (34). In short, OSI was calculated as the maximum directional response, ΔR_{max}, divided by the sum of responses in all other directions, $\Sigma\Delta R_{other}$ ($0 \leq OSI \leq 1$; 1 = perfectly orientation-tuned). DSI was calculated as ΔR_{max} divided by the sum of that direction and the antiparellel direction, $\Delta R_{maxr} + \Delta R_{orthogonal}$ ($0 \leq DSI \leq 1$; 1 = perfectly direction-tuned).

Statistical Analysis. All statistical analyses were performed in MATLAB. All datasets were first tested for normality (Lilliefors test), after which appropriate statistical tests were applied (e.g., *t* test/two-way ANOVA for normally distributed data, Mann–Whitney *U* test for nonparametric data). For comparisons of NFT versus non-NFT neuronal tuning in Fig. 3, two-way ANOVA was used to explore fixed effects due to interanimal and intra-animal differences. Data were analyzed by cell, grouped by mouse (i.e., Ms1, Ms2, or Ms3) and the presence of NFTs (i.e., NFT-bearing or non–NFT-bearing). For cohort-level analyses, the *P* value for the NFT group was used. For intra-animal comparisons, the interaction term was used (mouse × NFT presence) and the Tukey–Cramer post hoc test was used to explore intra-animal comparisons of NFT vs. non-NFT. The average *P* value for intraanimal comparisons of OSI and DSI was highly insignificant, $P = 0.47$.

Postmortem Whole-Brain Staining, Brain Clearing, and In Vivo Correlations. In a subset of rTg4510 mice, postmortem identification of NFTs was achieved using whole brain immunostaining followed by brain "clearing" (21). Immediately after in vivo recording of calcium levels, mice were perfused with 4% PFA in PBS, and brains were postfixed in 4% PFA for 1–2 d and then stored in 0.25% PFA at 4 °C. Whole brains were permeabilized and blocked in PBS containing 2% Triton-X100, 1% BSA, and 5% normal goat serum (NGS) for 5 h at room temperature. To immunolabel YC3.6-expressing cells and neurons with hyperphosphorylated tau, brains were incubated with primary antibodies [chicken anti-GFP (Invitrogen, 1:250) and mouse PHF1 (1:250)] in PBS containing 1% Triton, 1% BSA, and 2% NGS at 4 °C for 10 d. Secondary antibodies [goat anti-chicken Alexa Fluor 488 and goat anti-mouse Alexa Fluor 594 (Invitrogen, 1:250)] were applied for 7 d at 4 °C. For clearing, brains were stepwise saturated with glycerol by incubation in 80:20, 60:40, 40:60, and 20:80 PBS %:glycerol % for 5 h each at room temperature. Final clearing was achieved by incubation in a clearing solution of 53% benzyl alcohol, 45% glycerol, and 2% DABCO (wt/wt) for 10 d at room temperature. Clear brain multiphoton imaging (excitation $\lambda = 800$ nm) of previously in vivo imaged cells allowed for single cell reconstruction and correlation of PHF1-positive cells with measured calcium levels. To label mature NFTs, clear brains were then incubated in clearing solution containing 0.025% ThioS for 2 d at room temperature, followed by reclearing in clearing solution for 3 d. Reimaging the same cortical areas enabled reconstruction of NFT positions in in vivo images and correlation with calcium responses.

Immunolabeling of Visual Cortex Sections. Eight- to 9-mo-old rTg4510 and control mice were perfused with 4% PFA in PBS. Brains were postfixed in 4% PFA for 1–2 d at 4 °C, incubated for 2 d in 30% sucrose in PBS for cryoprotection, and then cut into 50-μm-thick coronal sections. Sections containing visual cortex were permeabilized with Triton-X100 in PBS, blocked in 5% NGS in PBS, and incubated in primary antibody [mouse anti-human tau (TAU-13; Abcam, 1:1,000)] in 5% NGS in PBS overnight at 4 °C. Secondary antibody [goat anti-mouse Cy3 (Invitrogen, 1:1,000)] was applied in 5% NGS in PBS for 1 h at room temperature. After washing in PBS, brain slices were mounted on microscope slides, and NFTs were stained with 0.025% ThioS in 50% ethanol for 8 min. ThioS was differentiated in 80% ethanol for 30s, sections were washed with water for 3 min, and coverslips were mounted using DAPI containing mounting medium (Vectashield).

ACKNOWLEDGMENTS. We thank Dr. Eloise Hudry and Dr. Michal Arbel-Ornath for helpful discussions and Dr. Peter Davies for the PHF1 antibody. This work was supported by the National Institutes of Health (Grants R01 AG026249, to B.T.H., and EB000768, to B.J.B.). S.W. was supported by the German Research Foundation. This research was conducted while M.L.A. was a recipient of a New Investigator Award in Alzheimer's Disease from the American Federation for Aging Research.

1. Grundke-Iqbal I, et al. (1986) Microtubule-associated protein tau: A component of Alzheimer paired helical filaments. *J Biol Chem* 261(13):6084–6089.
2. Hardy J, Duff K, Hardy KG, Perez-Tur J, Hutton M (1998) Genetic dissection of Alzheimer's disease and related dementias: Amyloid and its relationship to tau. *Nat Neurosci* 1(5):355–358.
3. Braak H, Braak E (1991) Neuropathological staging of Alzheimer-related changes. *Acta Neuropathol* 82(4):239–259.
4. Hutton M (2000) Molecular genetics of chromosome 17 tauopathies. *Ann N Y Acad Sci* 920:63–73.
5. Spires-Jones TL, Stoothoff WH, de Calignon A, Jones PB, Hyman BT (2009) Tau pathophysiology in neurodegeneration: A tangled issue. *Trends Neurosci* 32(3): 150–159.
6. Li X, et al. (2011) Novel diffusion barrier for axonal retention of Tau in neurons and its failure in neurodegeneration. *EMBO J* 30(23):4825–4837.
7. Bulic B, et al. (2009) Development of tau aggregation inhibitors for Alzheimer's disease. *Angew Chem Int Ed Engl* 48(10):1740–1752.
8. Schirmer RH, Adler H, Pickhardt M, Mandelkow E (2011) "Lest we forget you—methylene blue...". *Neurobiol Aging* 32(12):e7–e16.
9. Crimins JL, Rocher AB, Luebke JI (2012) Electrophysiological changes precede morphological changes to frontal cortical pyramidal neurons in the rTg4510 mouse model of progressive tauopathy. *Acta Neuropathol* 124(6):777–795.
10. Santacruz K, et al. (2005) Tau suppression in a neurodegenerative mouse model improves memory function. *Science* 309(5733):476–481.
11. Ghoshal N, et al. (2002) Tau conformational changes correspond to impairments of episodic memory in mild cognitive impairment and Alzheimer's disease. *Exp Neurol* 177(2):475–493.
12. Perez PD, et al. (2013) In vivo functional brain mapping in a conditional mouse model of human tauopathy (tau(P301L)) reveals reduced neural activity in memory formation structures. *Mol Neurodegener* 8:9.
13. Rocher AB, et al. (2010) Structural and functional changes in tau mutant mice neurons are not linked to the presence of NFTs. *Exp Neurol* 223(2):385–393.
14. Andermann ML, Kerlin AM, Roumis DK, Glickfeld LL, Reid RC (2011) Functional specialization of mouse higher visual cortical areas. *Neuron* 72(6):1025–1039.
15. Kuchibhotla KV, et al. (2008) Abeta plaques lead to aberrant regulation of calcium homeostasis in vivo resulting in structural and functional disruption of neuronal networks. *Neuron* 59(2):214–225.
16. Nagai T, Yamada S, Tominaga T, Ichikawa M, Miyawaki A (2004) Expanded dynamic range of fluorescent indicators for Ca(2+) by circularly permuted yellow fluorescent proteins. *Proc Natl Acad Sci USA* 101(29):10554–10559.
17. Kerlin AM, Andermann ML, Berezovskii VK, Reid RC (2010) Broadly tuned response properties of diverse inhibitory neuron subtypes in mouse visual cortex. *Neuron* 67(5): 858–871.
18. Hofer SB, et al. (2011) Differential connectivity and response dynamics of excitatory and inhibitory neurons in visual cortex. *Nat Neurosci* 14(8):1045–1052.
19. Menuet C, et al. (2012) Isoflurane anesthesia precipitates tauopathy and upper airways dysfunction in pre-symptomatic Tau.P301L mice: Possible implication for neurodegenerative diseases. *Neurobiol Dis* 46(1):234–243.
20. Grienberger C, et al. (2012) Staged decline of neuronal function in vivo in an animal model of Alzheimer's disease. *Nat Commun* 3:774.
21. Clendenon SG, Young PA, Ferkowicz M, Phillips C, Dunn KW (2011) Deep tissue fluorescent imaging in scattering specimens using confocal microscopy. *Microsc Microanal* 17(4):614–617.
22. Klunk WE, et al. (2002) Imaging Abeta plaques in living transgenic mice with multiphoton microscopy and methoxy-X04, a systemically administered Congo red derivative. *J Neuropathol Exp Neurol* 61(9):797–805.
23. Schön C, et al. (2012) Long-term in vivo imaging of fibrillar tau in the retina of P301S transgenic mice. *PLoS ONE* 7(12):e53547.
24. Higuchi M, Lee VM, Trojanowski JQ (2002) Tau and axonopathy in neurodegenerative disorders. *Neuromolecular Med* 2(2):131–150.
25. Spires TL, et al. (2006) Region-specific dissociation of neuronal loss and neurofibrillary pathology in a mouse model of tauopathy. *Am J Pathol* 168(5):1598–1607.
26. Fox LM, et al. (2011) Soluble tau species, not neurofibrillary aggregates, disrupt neural system integration in a tau transgenic model. *J Neuropathol Exp Neurol* 70(7): 588–595.
27. Cowan CM, Mudher A (2013) Are tau aggregates toxic or protective in tauopathies? *Front Neurol* 4:114.
28. Spires-Jones TL, Kopeikina KJ, Koffie RM, de Calignon A, Hyman BT (2011) Are tangles as toxic as they look? *J Mol Neurosci* 45(3):438–444.
29. Kopeikina KJ, Hyman BT, Spires-Jones TL (2012) Soluble forms of tau are toxic in Alzheimer's disease. *Transl Neurosci* 3(3):223–233.
30. Spillantini MG, Goedert M (2013) Tau pathology and neurodegeneration. *Lancet Neurol* 12(6):609–622.
31. Berger Z, et al. (2007) Accumulation of pathological tau species and memory loss in a conditional model of tauopathy. *J Neurosci* 27(14):3650–3662.
32. Lasagna-Reeves CA, et al. (2011) Tau oligomers impair memory and induce synaptic and mitochondrial dysfunction in wild-type mice. *Mol Neurodegener* 6:39.
33. de Calignon A, et al. (2010) Caspase activation precedes and leads to tangles. *Nature* 464(7292):1201–1204.
34. Andermann ML, Kerlin AM, Roumis DK, Glickfeld LL, Reid RC (2011) Functional specialization of mouse higher visual cortical areas. *Neuron* 72(6):1025–1039.